Available online at www.sciencedirect.com
SCIENCE DIRECT
Journal of Magnetic Resonance 179 (2006) 263–272
JMR Journal of Magnetic Resonance
www.elsevier.com/locate/jmr

Optimization of data acquisition for EPR imaging

Rizwan Ahmad [a], Bradley Clymer [a,b], Yuanmu Deng [c], Guanglong He [c], Deepti Vikram [c], Periannan Kuppusamy [c,*], Jay L. Zweier [c]

[a] Department of Electrical and Computer Engineering, The Ohio State University, College of Engineering, Columbus, Ohio 43210, USA
[b] Department of Biomedical Engineering, The Ohio State University, College of Engineering, Columbus, Ohio 43210, USA
[c] Center for Biomedical EPR Spectroscopy and Imaging, Davis Heart and Lung Research Institute, Department of Internal Medicine, The Ohio State University, College of Medicine, Columbus, Ohio 43210, USA

Received 23 October 2005; revised 24 December 2005
Available online 2 February 2006

Abstract

In electron paramagnetic resonance imaging (EPRI), long data acquisition time is one of the major problems limiting successful and useful biological EPRI experiments. Depending on the configuration (spatial distribution of paramagnetic species), information embedded in some objects can be characterized using a smaller number of projections, while others may require significantly larger number of projections to generate similar results. In order to optimize the acquisition process, it is therefore important to acquire a different number of projections for different objects. In this paper, a prediction scheme is demonstrated that can determine the number of projections required to achieve a preset reconstruction quality for a given object. After acquiring first few projections, corresponding partially filled *k*-space is analyzed. The complexity of data (to interpolate) in *k*-space is quantified and used to predict the number of required projections. All the projections are acquired using a mean-square difference-based adaptive acquisition technique that is also demonstrated in this work. The purpose of this non-uniform acquisition is to reduce redundancy in the acquired data which in turn decreases the number of projections required for the given object. It is also demonstrated that the performance of non-uniform acquisition is content dependant, and for certain configurations it may not be as effective as uniform acquisition in preserving signal from low intensity regions. The prediction scheme along with the non-uniform acquisition is tested using computer simulations, imaging of experimental phantoms, and in vivo imaging. Results indicate that the proposed method may save up to 50% of acquisition time. The techniques in this manuscript are described for 2D spatial imaging but can be extended to 3D imaging.

Keywords: Adaptive EPRI; EPR image reconstruction; Non-uniform projection acquisition

1. Introduction

The technique of EPRI has evolved over the past two decades to become an important tool for studying free radicals in many branches of science [1–8]. In the past few years, the potential applications of EPRI to studies of living biological systems have been recognized [9–17]. However, the broad application of the EPRI techniques to obtain high quality images of biological samples has been limited by several factors, including gradient magnitude and accuracy, sensitivity, and speed of acquisition [18]. In fact, slow data acquisition is one of the limiting factors in obtaining the high resolution images especially in the case of living systems where conditions may change with time. Efforts have been made to reduce the acquisition time [19–22]. Focus of this research is the optimization of acquisition process for EPRI.

EPRI is typically performed through reconstruction of projections [1,23]. Reconstruction quality depends on a number of factors such as the signal-to-noise ratio (SNR) of acquired data, sensitivity of the system, field homogeneity, and total number of acquired projections. In general, the reconstruction quality can be improved by acquiring more projections, but projection acquisition can be time consuming. In addition, the improvement in the reconstruction

* Corresponding author. Fax: +614 292 8454.
E-mail address: kuppusamy.1@osu.edu (P. Kuppusamy).

1090-7807/$ - see front matter © 2006 Elsevier Inc. All rights reserved.
doi:10.1016/j.jmr.2005.12.013

quality, due to an additional projection, becomes more and more marginal as we increase the number of acquired projections. This is due to the fact that for an extremely small angular spacing, adjacent projections tend to be nearly identical, and the acquisition of any additional projection would not contribute any distinct information. Therefore, acquiring projections beyond the limit where improvement becomes marginal can be a waste of time and resources. It is interesting to note that the reconstruction quality of different objects, depending on their configuration, converges at different rates, which implies that different objects may require different number of projections (N) to generate similar results. Therefore, data acquisition time can be considerably reduced if we could predict the optimum number of projections (N_o) for a given object. As a result, we can avoid acquiring projections more than what is required to achieve a preset reconstruction quality for the object under study.

Second, it has been shown that not all projections contain same amount of information [24–27]. Some projections, depending on the configuration of the object, contain vital information while others contain insignificant or redundant information. Previously, an adaptive scheme for non-uniform data acquisition has been proposed [28] where total number of acquired projections can be reduced by acquiring more informative set of projections. The scheme provides a better choice of projections than that with the acquisition at a uniform polar raster, but it does not demonstrate how many projections are required for a given reconstruction quality. In this research, the previously proposed technique for non-uniform acquisition is revisited but here the selection of projection angles is based on mean-square difference rather than entropy difference [29] between adjacent projections. Any non-uniform adaptive acquisition technique, however, has limited applications if there is no effective criterion to terminate the process of acquisition. Therefore, the proposed non-uniform data acquisition technique is incorporated with a prediction scheme that is also demonstrated in this paper. This prediction scheme, after partial data acquisition, can estimate the number of projections required for a given reconstruction quality which is defined in terms of mean-square-error (MSE) convergence rate, thus enabling us to terminate the acquisition process when the reconstruction quality has reached the predefined limit. Results from simulations and EPR imaging experiments illustrate that the prediction scheme is effective and reasonably accurate in estimating the number of required projections for the given configuration. It is important to mention that the main objective of this research is to reduce the acquisition time of EPR spatial imaging, and extension of the approach for spectral–spatial imaging is left for further studies.

2. Theory

2.1. Reconstruction methods

In EPR, images are typically reconstructed either by filtered back-projection (FBP) or by directly applying the Fourier slice theorem [23,30] in the spatial frequency domain and taking the inverse Fourier transform (IFT). In FBP, each projection is first filtered using some high pass filter and then projected back across the image space along lines orthogonal to the projection axis. On the other hand, in IFT-based method, n-dimensional frequency space (k-space) is constructed by taking the Fourier transform (FT) of corresponding one-dimensional projections and placing them in the n-dimensional k-space along proper orientations. Generally, local interpolation is used in k-space to arrange the data on a Cartesian grid. This interpolation error is the major source of reconstruction artifacts. After interpolation, we take the n-dimensional IFT of k-space to obtain the reconstructed image.

These FBP and IFT-based direct methods become mathematically equivalent in the limit when angular spacing between adjacent projections becomes small. However, actual implementation and hence performance of these two reconstruction schemes is different [31]. In general, FBP introduces false ridges and peaks [32] while the IFT-based direct method introduces circular blurring artifacts [33] especially in the regions away from the center of image domain. In this paper, we describe the implementation of the suggested prediction algorithm only using IFT-based direct image reconstruction although it can be extended for FBP.

2.2. Non-uniform acquisition

It has been shown [26] that two different sets of projections of the same object generate different results, even when the two sets have the same number of projections. This comes from the fact that different projections capture different amounts of information. In Fig. 1, vertical projection $\boldsymbol{p}_{0^\circ}(r)$ (obtained by integrating the phantom along vertical direction) reflects more information about the spatial distribution of paramagnetic species than the horizontal projection $\boldsymbol{p}_{90^\circ}(r)$ (obtained by integrating the phantom along horizontal direction). Entropy (distribution of data) can be used as a measure of information embedded in a projection. In fact, an entropy-based non-uniform projection acquisition scheme [28] has been suggested where the next projection is acquired between the two that present the maximum difference in the entropy function. Although entropy is an effective criterion to quantify information content of a projection, entropy difference between two projections, however, is not a robust criterion to determine the angle of new projection. For example, the entropy difference-based acquisition approach would not recommend acquiring a projection between two adjacent projections which exhibit smaller entropy difference. However, it is possible that two adjacent projections, which exhibit an entropy difference of zero, are entirely different in profile and capture distinct information. In other words, there can be a number of different functions with same entropy value. Therefore, entropy-based approach has a tendency to skip projections which carry distinct information. On

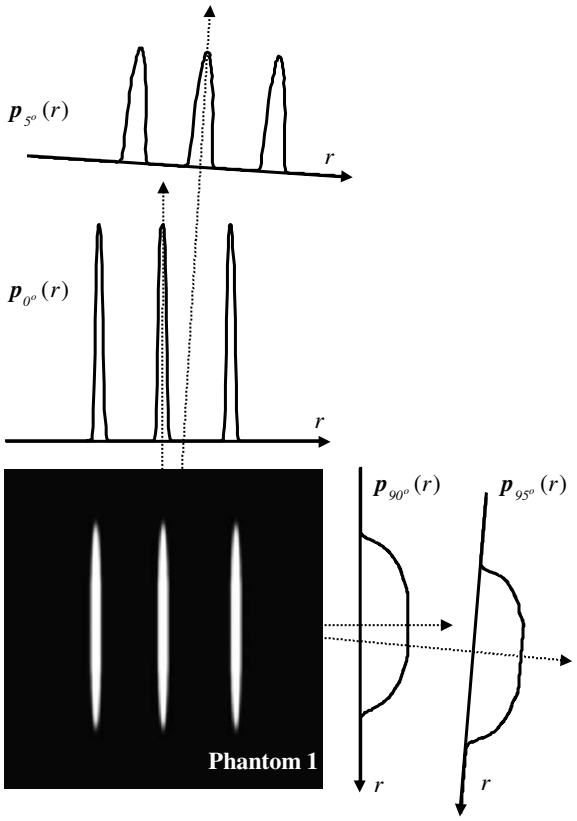

Fig. 1. Change is projection profile with a small change in acquisition angle. Vertical projection $\boldsymbol{p}_{0^\circ}(r)$ is displayed on the top while the horizontal projection $\boldsymbol{p}_{90^\circ}(r)$ is shown on the right of the simulated phantom. Here, r represents spatial coordinate. Change in projection profile for a 5° change in acquisition angle is also demonstrated. Projections $\boldsymbol{p}_{0^\circ}(r)$ and $\boldsymbol{p}_{5^\circ}(r)$ exhibit greater dissimilarity (or change) while projections $\boldsymbol{p}_{90^\circ}(r)$ and $\boldsymbol{p}_{95^\circ}(r)$ show much lesser dissimilarity.

the other hand, mean-square difference between adjacent projections effectively quantifies their dissimilarity, which is a measure of mutual information or redundancy. Mean-square difference-based approach, however, does not measure the information content of a projection directly. In Fig. 1, a 5° change in acquisition angle introduces substantial change in the vertical projection while a similar change in angle results in a marginal change for the horizontal projection. In other words, projection profile is changing rapidly around 0° direction and more gradually around 90° direction. Hence, an additional projection between $\boldsymbol{p}_{0^\circ}(r)$ and $\boldsymbol{p}_{5^\circ}(r)$ would contribute more towards improving reconstruction quality as compared to an additional projection acquired between $\boldsymbol{p}_{90^\circ}(r)$ and $\boldsymbol{p}_{95^\circ}(r)$.

The algorithm for non-uniform acquisition is stated below:

(1) Start with a small set of equally spaced projections. The angles corresponding to these projections are stored in a vector $\boldsymbol{\theta}$, and projections are stored in a matrix $\boldsymbol{P}$ where each column represents a projection. For example, the ith column of the matrix $\boldsymbol{P}$ represents the ith projection ($\boldsymbol{p}_i$) corresponding to the acquisition angle $\boldsymbol{\theta}_i$.

(2) Calculate the dissimilarity, d, between adjacent projections using Eqs. (1) and (2).

$$\boldsymbol{d}_i = (\boldsymbol{p}_{i+1} - \boldsymbol{p}_i)(\boldsymbol{\theta}_{i+1} - \boldsymbol{\theta}_i), \tag{1}$$

$$d_i = \|\boldsymbol{d}_i\|^2. \tag{2}$$

The value of d_i is suggestive of the dissimilarity between $(i+1)$th and ith projections. If two adjacent projections generate a larger d, it implies that data values are changing very rapidly between the two corresponding projection angles. The term $(\boldsymbol{\theta}_{i+1} - \boldsymbol{\theta}_i)$ in Eq. (1) makes sure that the angular difference between acquisitions is not too high, reducing probability that important projections are omitted.

(3) After calculating d between all adjacent projections, we collect a new projection between those two projections which show the largest dissimilarity, d. We insert the new projection and the corresponding angle in $\boldsymbol{P}$ and $\boldsymbol{\theta}$, respectively.

(4) Go back to (2) until we meet some criterion on total number of projections acquired. A scheme to terminate the acquisition process by predicting the optimum number of projections after partial acquisition is described later in the paper.

It is important to recognize that the performance of this non-uniform acquisition algorithm is content dependent. For some objects, this algorithm gives a substantial improvement, in terms of acquisition time, over the uniform acquisition technique, while for other objects the improvement is marginal. For example, consider a circular object at the center of projection space. All the projections for this object are identical and hence contain the same amount of information. As a result, a non-uniform acquisition technique does not give any improvement for such configurations. On the other hand, if our object is rod-shaped, non-uniform acquisition gives substantial improvement because the anisotropic nature of the rod makes the information content to be non-uniformly distributed among the projections. Although the above mentioned mean-square difference-based non-uniform acquisition approach does not measure the information content of projections directly, it assists us acquiring projections along the orientation where projection profile is changing the most with a minute change in acquisition angle. These projections are more likely to contribute distinct information and to make the reconstruction converge faster.

2.3. Prediction of number of projections

It is illustrated in Fig. 2 that reconstruction of different objects converges at different rates. Reconstruction quality and MSE for phantom 2 converge much faster and hence do not change considerably for acquisition beyond 15 projections, while reconstruction for phantom 3 exhibits slower convergence and improvement continues even after 30

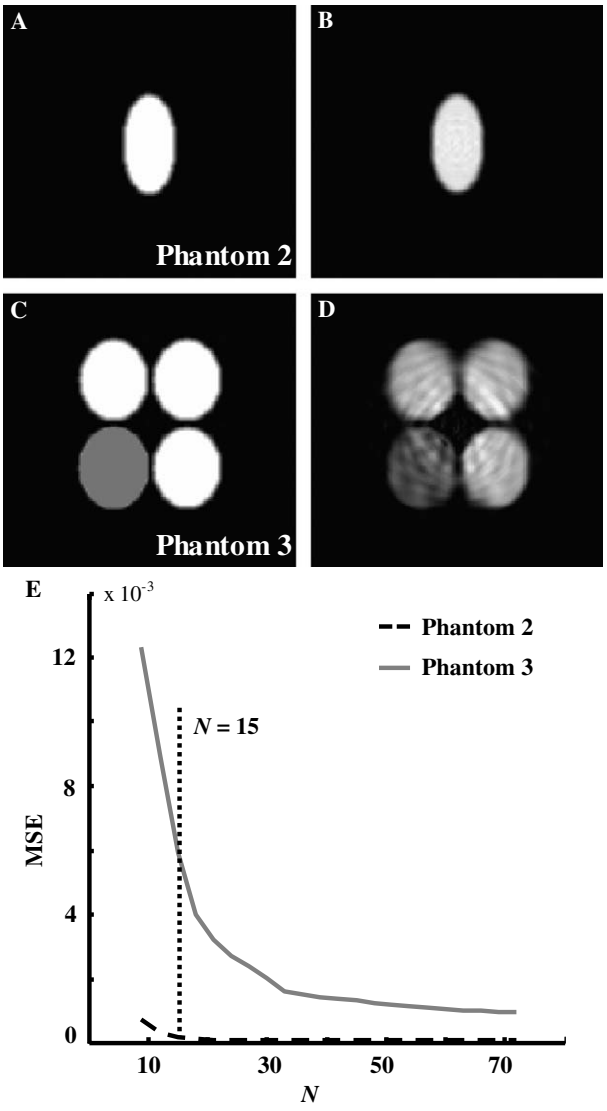

Fig. 2. Rate of mean-square-error (MSE) convergence for two different phantoms. (A) A simulated phantom. (B) IFT-based reconstructed image of (A) from 15 projections obtained by uniform acquisition technique. (C) A simulated phantom. (D) IFT-based reconstructed image of (C) from 15 projections obtained by uniform acquisition technique. (E) Convergence of MSE as a function of number of projections (N) for both phantoms.

projections. Therefore, for a given reconstruction quality, acquisition time can be saved by acquiring different number of projections for different objects. Hence, a scheme that can predict the optimum number of projections would be extremely useful. The previously proposed non-uniform scheme [28] would terminate acquisition at the point where entropy difference between adjacent projections is below a preset value. It usually results in an overestimated minimum number of projections. If the configuration of the object under study is known, total number of required projections can be calculated analytically using Nyquist–Shannon sampling theorem [34,35], but in practice we do not have the precise knowledge of object configuration. Therefore, we adopt an empirical approach in which the first 15 projections are acquired using the non-uniform acquisition technique and the corresponding partially filled k-space is analyzed and a complexity factor C is calculated which is suggestive of number of required projections. Below we discuss three main factors that are used to calculate C.

2.3.1. Spectral spread

Spectral spread (S), which measures the distribution of k-space data, is an important factor in estimating the number of required projections. In the IFT-based method for 2D spatial imaging, we take the FT of each individual projection and place it in 2D frequency space (k-space) at the orientation along which the projection was taken. This way, data are more concentrated at the center of 2D k-space and data get sparse as we move away from the center towards higher frequencies. If the k-space of an object shows considerable amount of energy in higher frequencies due to its sharp boundaries or fine details, we require more projections for such an object so that we have enough data to perform reasonable interpolation at the higher frequency region where data are less concentrated. If $\boldsymbol{F}_i$ is the discrete Fourier transform (DFT) of ith projection, and $\boldsymbol{G}_i$ represents the product (in frequency domain) of $\boldsymbol{F}_i$ and a high pass filter such as Ram-Lak, spectral spread S can be calculated using Eqs. (3) and (4).

$$G_i = \|\boldsymbol{G}_i\|^2, \tag{3}$$

$$S = \sum_{i=1}^{15} G_i. \tag{4}$$

In addition to object configuration, noise also affects the reconstruction convergence rate. Excessive noise slows down the convergence rate, and for such cases we require additional projections to achieve the same reconstruction quality. Value of S, however, also increases with the increase in noise. Therefore, spectral spread effectively takes into account the effects of noise. Similarly, linewidth of the absorption signal and the cutoff frequency [36] selected for deconvolution affect the convergence rate and hence the value of N_o, but the value of S, at the same time, get affected constructively to reflect the effects of these parameters values.

2.3.2. Local data variance in k-space

For IFT-based direct method, local interpolation applied in k-space is the major source of reconstruction artifacts. Extent of error introduced by interpolation depends directly on the spectral spread, S, and the extent of local variations in the values of k-space data. If data changes gradually over k-space, the interpolation in that space would be efficient, and consequently the error introduced by interpolation would be lower. On the other hand, a rapidly changing data in k-space would require more projections to increase the data density to keep the interpolation error in bounds.

Interpolation of data in k-space is generally based on Delaunay triangulation [37,38] in which the value at each point on a Cartesian grid is determined by the weighted

sum of the points in the nearest Delauny triangle. If the values of the points in that triangle have a large variance, it is likely to introduce large local interpolation error. A 2D variance matrix can be constructed by calculating the local variance of Delauny triangle data at each Cartesian point, and the 2D sum (V) of this variance matrix is directly related to the interpolation error and in turn to the number of required projections.

2.3.3. Anisotropy

To incorporate the non-uniform acquisition technique with the proposed prediction scheme, we take anisotropy (A) of k-space data spread of the object into account. Anisotropy of data spread in k-space is a measure of information distribution among projections. A perfectly isotropic k-space indicates that all projection angles are equally important while a highly anisotropic k-space suggests that information is localized primarily to a small subset of acquisition angles. As a result, the use of non-uniform acquisition technique for such cases can accelerate the MSE convergence rate. Eq. (5) represents a simple way of calculating the anisotropy of k-space data.

$$A = \frac{\max[G_i]}{\sum_{i=1}^{15} G_i}. \tag{5}$$

3. Results

3.1. Computational procedure

Twenty training phantoms were generated in MATLAB (MathWorks, Natick, MA, USA). To include the effects of noise, zero-mean white Gaussian noise was added to each projection before reconstructing the image. Strength of noise for each phantom was randomly selected so that SNR within the range of 20–100 was simulated. First, we constructed the number of projections (N) vs. MSE curve for each training phantom and calculated the rate of MSE decay (ΔMSE/ΔN). Number of required projections (N_o) is defined as the value of N where rate of convergence falls below a selected value ε. Hence, acquisition beyond N_o would improve the reconstruction quality at a rate lesser than ε. Value of ε reflects the desired reconstruction quality, and it can be selected according to the application or desired reconstruction quality. The resultant complexity factor (C) can be calculated by combining the above three parameters (S, V, and A) that control the interpolation error and hence the reconstruction convergence rate. The optimum combination of these parameters (shown in Eq. (6)) was empirically developed using computer simulations such that the correlation between C and N_o was maximized.

$$C = \frac{S \times V}{\sqrt[4]{A}}. \tag{6}$$

It is important to mention that C is calculated using the information of first 15 projections only. After calculating C for all the training phantoms, C vs. N_o curve was linear fit, and later we used this regression line (Eq. (7)) to predict N_o for the test phantoms. Predicted value of N_o is denoted by $\hat{N}_o$.

$$\hat{N}_o = X_1 C + X_0. \tag{7}$$

Here X_o and X_1 are the coefficients of regression line obtained by linear fitting C vs. N_o curve. In Fig. 3A, ○ indicates training phantom and the solid line shows the linear fit. A strong correlation between C and N_o suggests that C can be used to estimate N_o efficiently.

3.2. Simulations

In Fig. 4, the performances of uniform and non-uniform acquisitions are compared for the simulated phantom of Fig. 1. To compare the two acquisition methods under different conditions of noise, zero-mean white Gaussian noise of different variance was added to the theoretical projec-

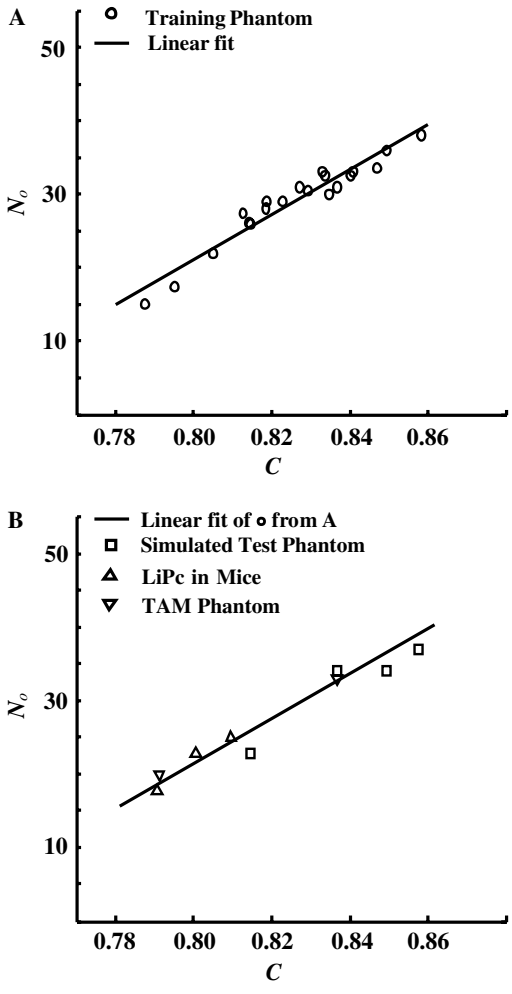

Fig. 3. Quantitative analysis of prediction algorithm. (A) Regression line obtained by linear fitting of the complexity factor (C) vs. optimum number of projections (N_o) curve for the simulated training phantoms. (B) N_o for simulated test phantoms (□), TAM phantoms (▽), and in vivo sample (△) tested against the regression line of (A). Vertical distances of □, ▽, and △ from the regression line indicate the error of prediction.

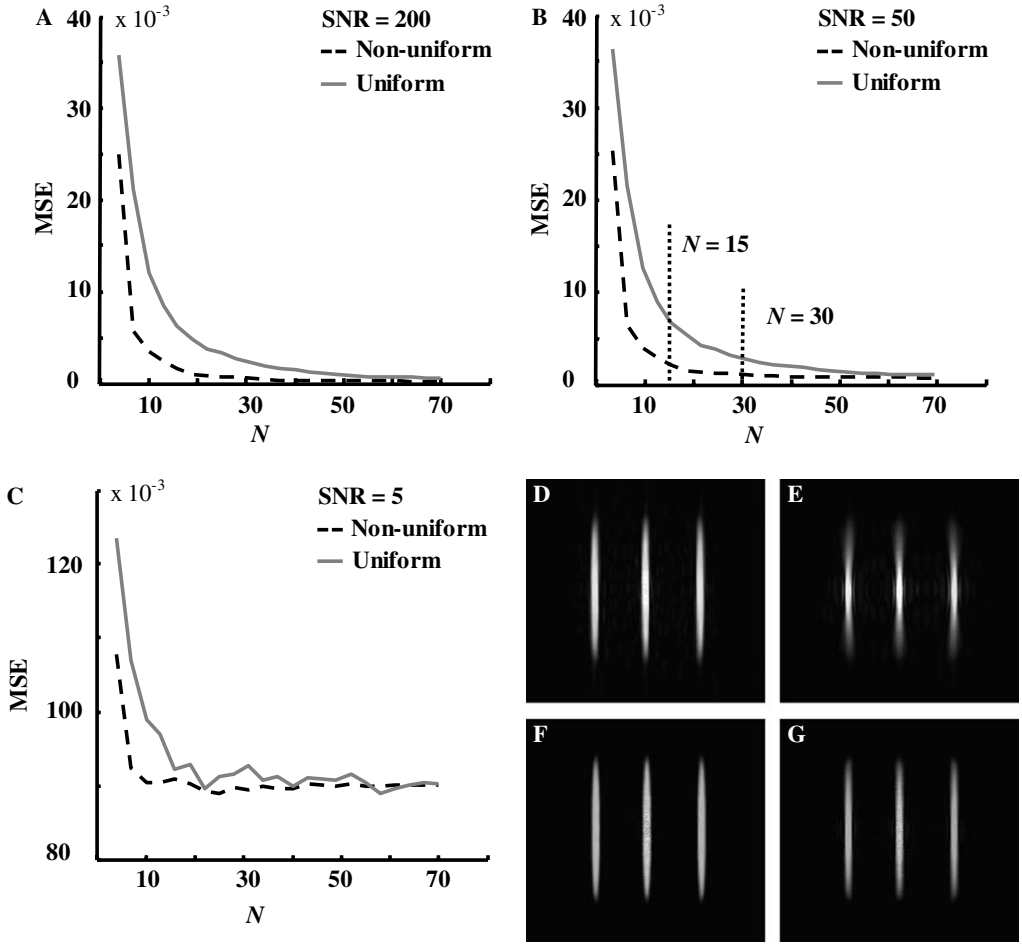

Fig. 4. Comparison of non-uniform and uniform acquisition techniques for different SNR values for the simulated phantom of Fig. 1. (A) SNR = 200. (B) SNR = 50. For MSE = 2×10^{-3}, uniform acquisition requires 32 projections and non-uniform acquisition requires 15 projections, which is an improvement of 53%. (C) SNR = 5. (D) Image reconstructed from 15 projections obtained by non-uniform acquisition for SNR = 50. (E) Image reconstructed from 15 projections obtained by uniform acquisition for SNR = 50. (F) Image reconstructed from 30 projections obtained by non-uniform acquisition for SNR = 50. (G) Image reconstructed from 30 projections obtained by uniform acquisition for SNR = 50.

tions. The resulting data sets had SNR of 200, 50, and 5. Here, SNR is defined as the ratio of peak-to-peak signal amplitude and the standard deviation of noise added to the projection. For each data set, SNR was calculated for the projection with least peak-to-peak signal amplitude. It is demonstrated in Fig. 4 that the above described non-uniform acquisition technique generates substantially lesser MSE as compared to uniform acquisition for a wide range of SNR. Here, MSE is defined as a mean-square difference between the original (reference) and reconstructed phantoms.

To test the accuracy of prediction scheme, four simulated test phantoms were generated using MATLAB. The values of C and N_o were calculated for each test phantom as it is described in the previous section. In Fig. 3B, □ indicates actual value of N_o (value of N where rate of MSE convergence falls below ε that is selected to be 4×10^{-5}) for simulated test phantoms, and the vertical distance of □ from the regression line is the error of prediction ($|N_o - \hat{N}_o|$). $\hat{N}_o$ can also be calculated using Eq. (7). Data for simulated test phantoms are reported in Table 1.

3.3. Phantom imaging experiment

Two phantoms were generated using capillary tubes filled with an aqueous solution containing 0.5 mM triarylmethyl (TAM) radical with an observed peak-to-peak linewidth of 220 mG under aerobic conditions. One of the phantoms was I-shaped while other was U-shaped. The longest physical dimension of these phantoms was limited to 7 mm. The phantoms were imaged on an S-band (2.2 GHz) EPRI system with a surface loop-gap resonator [39] with an inner diameter of 8 mm and an outer diameter of 10 mm. Sample was placed on the coil axis about 1 mm from its center. Sweep width was 5 G, and a gradient strength of 8 G/cm was applied. Field modulation was applied at 100 kHz, and the first derivative of EPR absorption line was detected with a lock-in amplifier. Modulation amplitude was set at 100 mG. A total of 256 projections were obtained with a scan time of 5.6 s per projection. The observed peak-to-peak SNR for zero-gradient projection was 64. No correction for non-uniform microwave field or sensitivity [40] was applied. Since the theoretical

Table 1
Optimum number of projections (measured and estimated) for all test cases

Configuration		C	Optimum number of projections		Error $\lvert N_o - \hat{N}_o \rvert$
			Observed (N_o)	Estimated ($\hat{N}_o$)	
Simulated phantoms	Test 1	0.8128	22	25	3
	Test 2	0.8552	36	38	2
	Test 3	0.8471	33	35	2
	Test 4	0.8346	33	32	1
TAM phantoms	U-shaped	0.8345	32	32	0
	I-shaped	0.7894	19	18	1
In vivo imaging	YZ	0.7988	22	21	1
	XZ	0.8077	24	24	0
	XY	0.7889	17	18	1

image of the phantom was not available, images reconstructed using 256 projections (acquired at uniformly spaced angles) were used as reference images to calculate MSE. Comparison of uniform and non-uniform acquisition methods is reported in Figs. 5 and 6.

For the evaluation of prediction scheme, we calculated C and N_o as explained in the previous section, and $\hat{N}_o$ was obtained by inserting the corresponding values of C in Eq. (7). Actual values (N_o) and predicted values ($\hat{N}_o$) are compared in Table 1. In Fig. 3B, ∇ indicates actual value of N_o for experimental phantoms, and the vertical distance of ∇ from regression line reflects the error of prediction. It is shown that for the I-shaped phantom, $\hat{N}_o$ is within 1 projection of N_o, and for the U-shaped phantoms, $\hat{N}_o$ and N_o are equal.

3.4. Imaging in vivo

Animal studies were done using the approved protocol of Institutional Laboratory Animal Care and Use Committee at The Ohio State University. Five mice were used in the study. One million RIF-1 (radiation-induced fibro sarcoma) cells were implanted in the subcutaneous tissue of the hind limb. The tumors were allowed to grow for one week. After this period, the tumors were approximately $309.9 \pm 27.5\ \text{mm}^3$ in size. Xylazine/ketamine (90 mg/kg bw) was given intraperitoneally before imaging. The procedure for implanting LiPc crystals was followed according to Ilangovan et al. [41] where about 10 μg of microcrystalline powder of LiPc was placed in a 22-gauge needle and a thin wire was used to push the crystals into the tumor after the needle was inserted into the tumor on the right hind limb. Implantation was carried out on three locations on the tumor. At the end of experiments, the animals were sacrificed by cervical dislocation. EPR measurements were taken on an L-band (1.1 GHz) EPR spectrometer [17] with a surface loop-gap resonator [42] with inner diameter of 10 mm and outer diameter of 13.5 mm. Sample was placed on the coil axis about 1.5 mm from its center. Spectrometer settings were: incident microwave power: 210 μW (B1 ≈ 11 mG), sweep width: 2 G, modulation frequency: 100 kHz, modulation amplitude: 50 mG. Observed linewidth was 100 mG, and observed peak-to-peak SNR for zero-gradient projection was 40. Three sets of data, each corresponding to one of the three 2D orthogonal orientations (named *yz*, *xz*, and *xy*) were obtained with each data set containing a total of 128 projections. Acquisition time for each projection was set to 4 s. Fig. 7 displays the reconstructions based on uniform and non-uniform acquisitions.

For the prediction scheme, values of C and N_o corresponding to *yz*, *xz*, and *xy* orientations were calculated as explained in the previous section. In Fig. 3B, $\triangle$ indicates actual value of N_o, and the vertical distance of $\triangle$ from the linear fit line represents error of estimation ($\lvert N_o - \hat{N}_o \rvert$), which is also documented in Table 1.

4. Discussion

The advantage of using the suggested optimization scheme is twofold. First, the non-uniform acquisition technique optimizes the information content of the measured data and hence enables the reconstruction process to converge faster. Fig. 4 shows that for $\text{SNR} = 50$ and $\text{MSE} = 2 \times 10^{-3}$, uniform acquisition requires 32 projections, while non-uniform acquisition requires only 15 projections, an improvement of more than 50%. Noticeable improvement for non-uniform acquisition is also illustrated from phantom imaging results shown in Figs. 5 and 6. In the case of biological sample, on the other hand, the improvement is relatively moderate as it is demonstrated in Fig. 7. Here, 30 uniformly acquired projections give same MSE as 22 projections acquired using proposed non-uniform scheme. It is an improvement of around 27%.

It is worth mentioning that non-uniform acquisition schemes, including the one mentioned in this paper, tend to be more effective in preserving the stronger signals while the weaker signals get suppressed. In other words, the reconstruction of a sample region where signal is strong converges faster while the reconstruction of a sample region with weaker signal takes extra time to converge. This limitation of the non-uniform acquisition is also demonstrated in Fig. 7. Thus, the non-uniform acquisition scheme should be used with caution in the situations where the faint details are of significance.

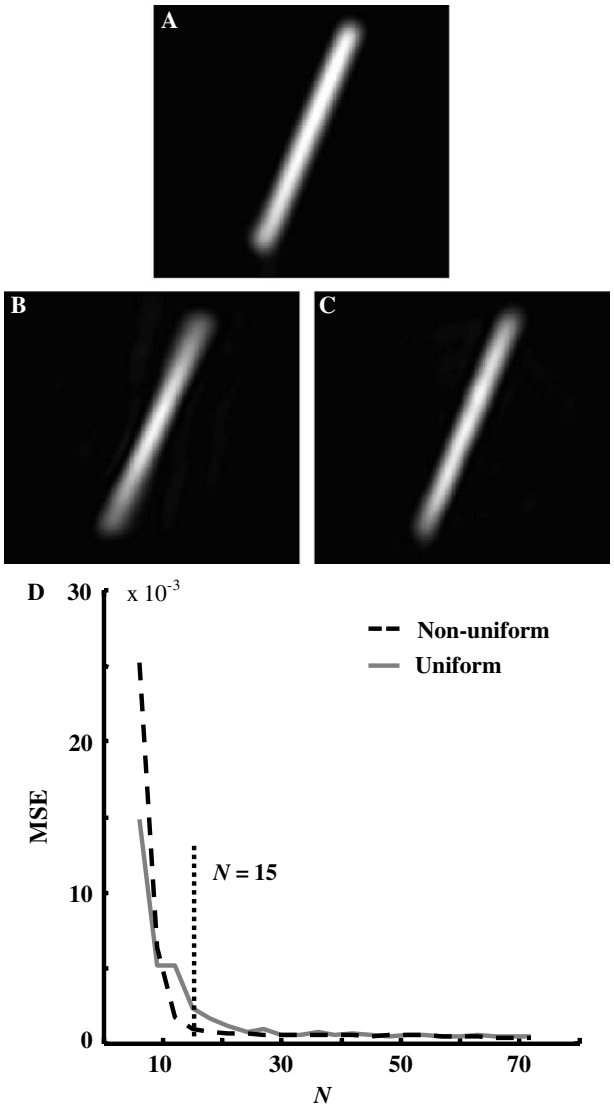

Fig. 5. Imaging of TAM solution in an I-shaped capillary tube. (A) Reference image reconstructed from 256 projections acquired by uniform acquisition. (B) Image reconstructed from 15 projections obtained by uniform acquisition. (C) Image reconstructed from 15 projections obtained by non-uniform acquisition. (D) Convergence of mean-square-error (MSE) as a function of number of projections (N) for both uniform and non-uniform acquisitions. For MSE $= 1.0 \times 10^{-3}$, uniform acquisition requires 24 projections while mean-square difference-based non-uniform acquisition requires 15 projections, which is an improvement of 38%.

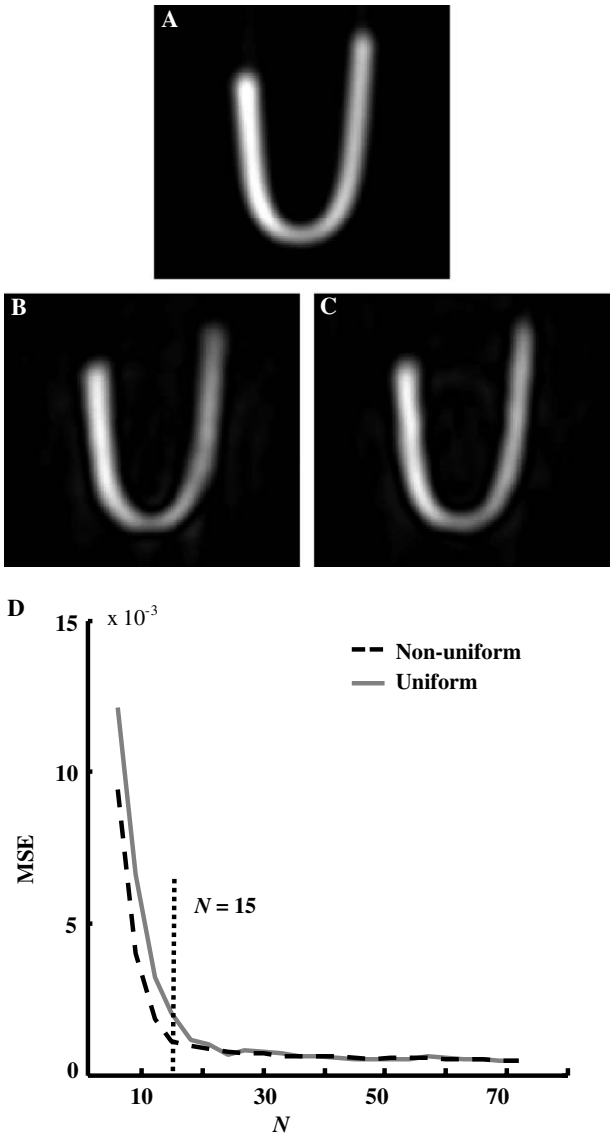

Fig. 6. Imaging of TAM solution in a U-shaped capillary tube. (A) Reference image reconstructed from 256 projections acquired by uniform acquisition. (B) Image reconstructed from 15 projections obtained by uniform acquisition. (C) Image reconstructed from 15 projections obtained by non-uniform acquisition. (D) Convergence of mean-square-error (MSE) as a function of number of projections (N) for both uniform and non-uniform acquisitions. For MSE $= 1.0 \times 10^{-3}$, uniform acquisition requires 19 projections while mean-square difference-based non-uniform acquisition requires 15 projections, which is an improvement of 21%.

In addition to the non-uniform acquisition, the algorithm demonstrated in this paper can efficiently predict the number of required projections for a given object. Table 1 indicates that the simulated phantom Test 1 requires 22 projections for a preset reconstruction quality ($\varepsilon = 4 \times 10^{-5}$) while the simulated phantom Test 2 requires 36 projections to generate similar results. The proposed prediction algorithm suggests 25 projections for Test 1 and 38 projections for Test 2. A typical approach, on the other hand, would be to use a same conservative estimate of number of projections for all the phantoms. For example, for 2D spatial imaging it is a common practice to acquire more than 30 projections regardless of the object configuration. Hence, by using this prediction technique alone (without considering non-uniform acquisition), we can save about 50% of projections. The simulation and experimental results (Table 1) indicate that the proposed algorithm can predict the number of required projections with reasonable accuracy even in the presence of regular levels of noise. It is a robust approach and gives reasonable performance for both simple and complex configurations. A standard deviation of prediction error ($|N_o - \hat{N}_o|$) for all test cases, simulated and experimental, is only 1.5 projections.

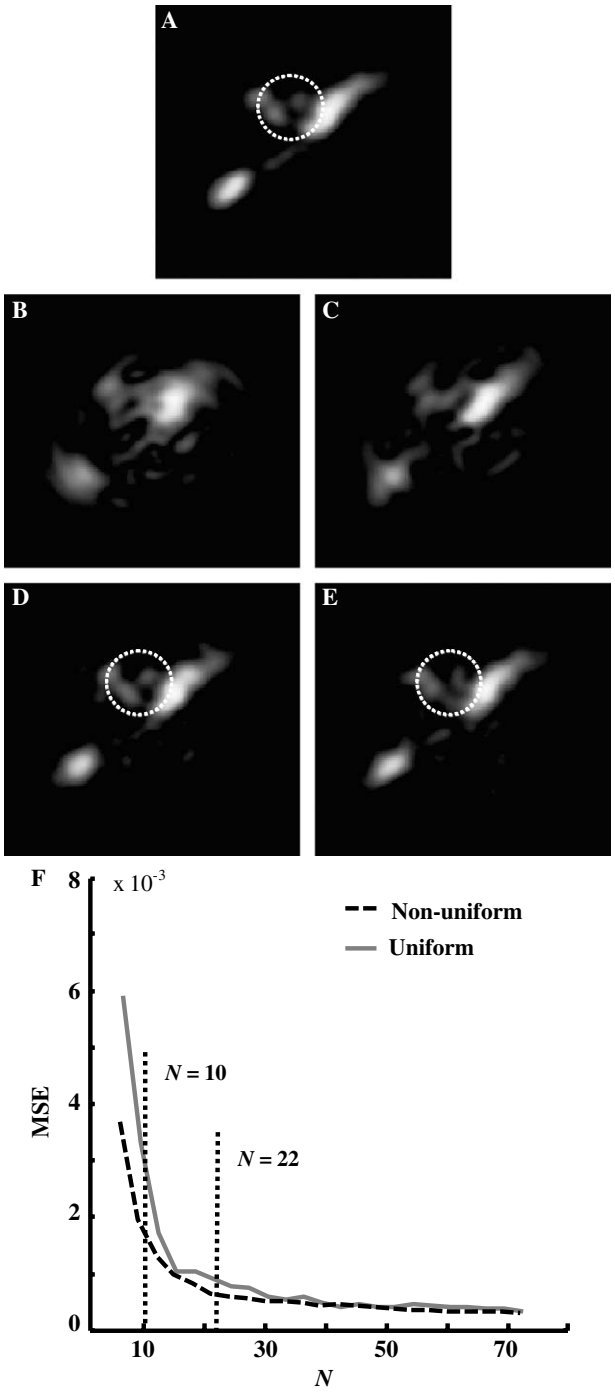

Fig. 7. One of the three 2D images of LiPc embedded in three locations in the tumor grown on mice leg. (A) Reference image reconstructed from 128 projections acquired by uniform acquisition. (B) Image reconstructed from 10 projections obtained by uniform acquisition. (C) Image reconstructed from 10 projections obtained by non-uniform acquisition. (D) Image reconstructed from 22 projections obtained by uniform acquisition. (E) Image reconstructed from 22 projections obtained by non-uniform acquisition. (F) Convergence of mean-square-error (MSE) as a function of number of projections (N) for both uniform and non-uniform acquisitions. For $\mathrm{MSE} = 0.6 \times 10^{-3}$, uniform acquisition requires 30 projections while mean-square difference-based non-uniform acquisition requires 22 projections which is an improvement of 27%. It is evident that non-uniform acquisition has out-performed uniform acquisition in the over all reconstruction quality, but visual inspection of the section of reconstructed image that resides inside the dotted circle suggests that non-uniform acquisition is not as effective in preserving the weaker signal.

It typically takes several minutes for a conventional EPR imaging system to acquire a 2D image and even an hour or longer for a 3D image [18]. The optimization scheme suggested in this paper can considerably reduce the acquisition time which can be vital for many biological applications.

5. Conclusions

We have suggested and tested a scheme that can predict the number of projections required for a given object by using the information of the first few projections. After acquiring the initial projections, we analyze the partially filled k-space and make a prediction of total number of required projections based on various spectral and anisotropic characteristics of partially filled k-space. An accurate prediction ensures that for different objects we acquire different number of projections that is optimum for their configurations. Therefore, we can avoid acquiring the same conservative number of projections for all objects. We have demonstrated that this scheme can save as much as 50% of the data acquisition time. This savings in acquisition time can be critical for biological applications where conditions may change over time. In addition, simulated and experimental data indicate that acquiring projections at non-uniform angular raster increases the rate of convergence. Hence, the process of data acquisition is optimized even further by incorporating the non-uniform acquisition technique with the prediction scheme described in this paper. Results of computer simulations, phantom imaging experiment, and in vivo imaging suggest that the performance of the proposed scheme is consistent for a wide range of SNR.

Acknowledgments

This work was supported by NIH Research Grants EB000591 and EB005004. We thank S. Petryakov for technical assistance.

References

[1] G.R. Eaton, S.S. Eaton, K. Ohno, EPR Imaging and In Vivo EPR, CRC Press, Boca Raton, 1991.
[2] S.S. Eaton, G.R. Eaton, EPR imaging, Spectroscopy (1986).
[3] U. Ewert, T. Herrling, Spectrally-resolved EPR tomography with stationary gradient, Chem. Phys. Lett. 129 (1986) 516–517.
[4] M.M. Maltempo, S.S. Eaton, G.R. Eaton, Spectral-spatial two-dimensional EPR imaging, J. Magn. Reson. 72 (1987) 449.
[5] K. Ohno, ESR imaging, Magn. Reson. Rev. 11 (1987) 275.
[6] S.S. Eaton, M.M. Maltempo, E.D.A. Stemp, G.R. Eaton, Three-dimensional EPR imaging with one spectral and two spatial dimensions, Chem. Phys. Lett. 142 (1987) 567–569.
[7] U. Ewert, T. Herrling, W. Schneider, EPR imaging in Magnetic resonance and related phenomena, in: 24th Ampere Conference, 1988.
[8] T. Miki, M. Ikeya, A method of EPR imaging for differential detection of paramagnetic species distribution utilizing localized field modulation, J. Magn. Reson. 80 (1988) 502.
[9] L.J. Berliner, H. Fujii, X. Wan, S.J. Lukiewicz, Feasibility study of imaging a living murine tumour by electron paramagnetic resonance, Magn. Reson. Med. 4 (1987) 380.

[10] H.J. Halpern, D.P. Spencer, J.V. Polen, M.K. Bowman, A.C. Nelson, E.M. Dowey, E.A. Teicher, Imaging radio frequency electron-spin resonance spectrometer with high resolution and sensitivity for in vivo measurements, Rev. Sci. Instrum. 60 (1989) 1040.
[11] R.K. Woods, J.W. Dobrucki, J.F. Glockner, P.D. Morse II, H.M. Swartz, Spectral-spatial ESR imaging as a method of noninvasive biological oximetry, J. Magn. Reson. 85 (1989) 50.
[12] H. Katsuda, T. Kobayashi, H. Saito, T. Matsunaga, M. Ikeya, Electron spin resonance imaging of mouse B16 melanoma, Chem. Pharm. Bull. (Tokyo) 38 (1990) 2838–2840.
[13] J.W. Dobrucki, F. Demsar, T. Walczak, R.K. Woods, G. Bacic, H.M. Swartz, Electron spin resonance microscopy of an in vitro tumor model, Br. J. Cancer 61 (1990) 221–224.
[14] M. Alecci, S. Colacicchi, P.L. Indovina, F. Momo, P. Pavone, A. Sotgiu, Three-dimensional in vivo ESR imaging in rats, Magn. Reson. Imaging 8 (1990) 59–63.
[15] J.W. Dobrucki, R.M. Sutherland, H.M. Swartz, Nonperturbing test for cytotoxicity in isolated cells and spheroids, using electron paramagnetic resonance, Magn. Reson. Med. 19 (1991) 42.
[16] V. Quaresima, M. Alecci, M. Ferrari, A. Sotgiu, Whole rat electron paramagnetic resonance imaging of a nitroxide free radical by a radiofrequency (280 MHz) spectrometer, Biochem. Biophys. Res. Commun. 183 (1992) 829.
[17] P. Kuppusamy, P. Wang, J.L. Zweier, Three-dimensional spatial EPR imaging of the rat heart, Magn. Reson. Med. 34 (1995) 99–105.
[18] P. Kuppusamy, M. Chzhan, J.L. Zweier, Developement and optimization of three-dimensional spatial EPR imaging for biological organs and tissues, J. Magn. Reson. 106 (1995) 122–130.
[19] F. Demsar, T. Walczak, P.D. Morse II, G. Bacic, Z. Zolnai, H.M. Swartz, Detection of diffusion and distribution of oxygen by fast-scan EPR imaging, J. Magn. Reson. 76 (1988) 224–331.
[20] Y. Deng, G. He, S. Petryakov, P. Kuppusamy, J.L. Zweier, Fast EPR imaging at 300 MHz using spinning magnetic field gradients, J. Magn. Reson. 168 (2004) 220–227.
[21] J.P. Joshi, J.R. Ballard, G.A. Rinard, R.W. Quine, S.S. Eaton, Rapid-scan EPR with triangular scans and fourier deconvolution to recover the slow-scan spectrum, J. Magn. Reson. 175 (2005) 44–51.
[22] J.W. Stoner, D. Szymanski, S.S. Eaton, R.W. Quine, G.A. Rinard, Direct-detected rapid-scan EPR at 250 MHz, J. Magn. Reson. 170 (2004) 127–135.
[23] S. Lin, C. Fuh, Range data reconstruction using Fourier slice theorem, Proc. IEEE Int'l Conf. Pattern Recogn. 1 (1996) 874–878.
[24] A.M. Comrack, Reconstruction of densities from their projections, with application in radiological physics, Phys. Med. Biol. 18 (1973) 195–207.
[25] P.C. Lauterbur, Image formation by induced local interactions: examples employing nuclear magnetic resonance, Nature 242 (1973) 190–191.
[26] I.G. Kazantsev, Projection information content, Inverse Problems 7 (1991) 887–898.
[27] Y. Deng, P. Kuppusamy, J.L. Zweier, Progressive EPR imaging with adaptive projection acquisition, J. Magn. Reson. 174 (2005) 177–187.
[28] G. Placidi, M. Alecci, A. Sotgiu, Theory of adaptive acquisition method for image reconstruction from projections and application to EPR imaging, J. Magn. Reson. 108 (1995) 55–57.
[29] L. Brillouin, Science and Information Theory, second ed., 1963.
[30] G. Hall, T.J. Terrell, J.M. Senior, L.M. Murphy, New fast discrete Radon transform for enhancing linear features in noisy images, Trans. IEE Electronics Lett. 24 (1988) 876–877.
[31] G. Placidi, M. Alecci, S. Colacicchi, A. Sotgiu, Fourier reconstruction as a valid alternative to filtered back projection in iterative applications: implementation of fourier spectral spatial EPR imaging, J. Magn. Reson. 134 (1998) 280–286.
[32] E. Kupce, R. Freeman, Fast multidimensional NMR: radial sampling of evolution space, J. Magn. Reson. 173 (2005) 317–321.
[33] M. Magnusson, P.-E. Danielsson, P. Edholm, Artefacts and remedies in direct Fourier tomographic reconstruction, in: Proceedings of IEEE Conference on Nuclear Science Symposium and Medical Imaging 2 (1992) 1138–1140.
[34] H. Nyquist, Certain topics in telegraph transmission theory, Trans. AIEE 47 (1928) 617–644.
[35] R.C. Dorf, The Electrical Engineering Handbook, CRC Press, Ann Arbor, 1993.
[36] H. Hirata, T. Itoh, K. Hosokawa, Y. Deng, H. Susaki, Systematic approach to cutoff frequency selection in continuous-wave electron paramagnetic resonance imaging, J. Magn. Reson. 175 (2005) 177–184.
[37] L. De Floriani, A pyramidal data structure for triangle-based surface description, Trans. IEEE Comput. Graph. Appl. 9 (1989) 67–68.
[38] L. Rognant, J.M. Chassery, S. Goze, J.G. Planes, The Delaunay constrained triangulation: the Delaunay stable algorithms, Proc. IEEE Int'l Conf. Information Visualization (1999) 147–152.
[39] S. Petryakov, M. Chzhan, A. Samouilov, G. He, P. Kuppusamy, A bridged loop–gap S-band surface resonator for topical EPR spectroscopy, J. Magn. Reson. 151 (2001) 124–128.
[40] G. He, S.P. Evalappan, H. Hirata, Y. Deng, S. Petryakov, P. Kuppusamy, J.L. Zweier, Mapping of the B1 field distribution of a surface coil resonator using EPR imaging, Magn. Reson. Med. 48 (2002) 1057–1062.
[41] G. Ilangovan, J.L. Zweier, P. Kuppusamy, Mechanism of oxygen-induced EPR line broadening in lithium phthalocyanine microcrystals, J. Magn. Reson. 170 (2004) 42–48.
[42] H. Hirata, T. Walczak, H.M. Swartz, Characteristics of an electronically tunable surface-coil-type resonator for L-band electron paramagnetic resonance spectroscopy, Rev. Sci. Instrum. 72 (2001) 2839–2841.